1 **Anthropogenic influences on the physical state of submicron particulate**

2 **matter over a tropical forest**

3
4
5 Adam P. Bateman[1], Zhaoheng Gong[1], Tristan H. Harder[2], Suzane S. de Sá[1], Bingbing Wang[3,4],
6 Paulo Castillo[5], Swarup China[3], Yingjun Liu[1], Rachel E. O'Brien[2,6], Brett Palm[7], Hung-Wei
7 Shiu[3], Glauber da Silva[8], Ryan Thalman[5], Kouji Adachi[9], M. Lizabeth Alexander[3], Paulo
8 Artaxo[10], Allan K. Bertram[11], Peter R. Buseck[12], Mary K. Gilles[2], Jose L. Jimenez[7], Alexander
9 Laskin[3], Antonio O. Manzi[8], Arthur Sedlacek[5], Rodrigo A. F. Souza[13], Jian Wang[5], Rahul
10 Zaveri[3], Scot T. Martin[*1,14]
11
12 [1]School of Engineering and Applied Sciences, Harvard University, Cambridge, Massachusetts,
13 USA
14 [2]Chemical Sciences Division, Lawrence Berkeley National Laboratory, Berkeley, CA, USA
15 [3]William R. Wiley Environmental Molecular Sciences Laboratory, Pacific Northwest National
16 Laboratory, Richland, WA, USA
17 [4]State Key Laboratory of Marine Environmental Science, College of Ocean and Earth Sciences,
18 Xiamen University, Xiamen, China
19 [5]Brookhaven National Laboratory, Upton, New York, USA
20 [6]Department of Civil and Environmental Engineering, Massachusetts Institute of Technology,
21 Cambridge, Massachusetts, USA
22 [7]University of Colorado, Boulder, USA
23 [8]National Institute of Amazonian Research, Amazonas, Brazil
24 [9]Atmospheric Environment and Applied Meteorology Research Department, Meteorological
25 Research Institute, Tsukuba, Ibaraki, Japan
26 [10]University of São Paulo, São Paulo, Brazil
27 [11]Department of Chemistry, University of British Columbia, Vancouver, BC, Canada
28 [12]School of Earth and Space Exploration & School of Molecular Sciences, Arizona State
29 University, Tempe, Arizona, USA
30 [13]Amazonas State University, Amazonas, Brazil
31 [14]Department of Earth and Planetary Sciences, Harvard University, Cambridge, Massachusetts,
32 USA
33
34 *Atmospheric Chemistry and Physics*

35

36

37

38 [*] Correspondence to: S.T. Martin (scot_martin@harvard.edu)

Atmospheric
Chemistry
and Physics
Discussions

39   **Abstract**

40   The occurrence of non-liquid and liquid physical states of submicron atmospheric

41   particulate matter (PM) downwind of an urban region in central Amazonia was investigated.

42   Measurements were conducted during two Intensive Operating Periods (IOP1 and IOP2) that

43   took place during the wet and dry seasons, respectively, of the GoAmazon2014/5 campaign. Air

44   masses representing variable influences of background conditions, urban pollution, and regional

45   and continental scale biomass burning passed over the research site. As the air masses varied,

46   particle rebound fraction, which is an indicator of the mix of physical states in a sampled particle

47   population, was measured in real time at ground level using an impactor apparatus. Micrographs

48   collected by transmission electron microscopy confirmed that liquid particles adhered while non-

49   liquid particles rebounded. Relative humidity (RH) was scanned to collect rebound curves. When

50   the apparatus RH matched ambient RH, 95% of the particles were liquid as a campaign average,

51   although this percentage dropped to as low as 60% during periods of anthropogenic influence.

52   Secondary organic material, produced for the most part by the oxidation of volatile organic

53   compounds emitted from the forest, was the largest source of liquid PM. Analyses of the mass

54   spectra of the atmospheric PM by positive-matrix factorization (PMF) and of concentrations of

55   carbon monoxide, total particle number, and oxides of nitrogen were used to identify time

56   periods affected by anthropogenic influences, including both urban pollution and biomass

57   burning. The occurrence of non-liquid PM correlated with these indicators of anthropogenic

58   influence. A linear model having as output the rebound fraction and as input the PMF factor

59   loadings explained up to 70% of the variance in the observed rebound fractions. Anthropogenic

60   influences appear to favor non-liquid PM by providing molecular species that increase viscosity

Atmospheric
Chemistry
and Physics
Discussions

Open Access

61   when internally mixed with background PM, by contributing non-liquid particles in external

62   mixtures of PM, and a by combination of these effects under real-world conditions.

Atmospheric
Chemistry
and Physics
Discussions

Open Access

EGU

1. Introduction

63

64   Particulate matter (PM) directly affects the Earth's climate by scattering and absorbing

65 solar radiation and indirectly by effects on clouds (Ramanathan et al., 2001). The magnitude of

66 these effects depends in part on the physical and chemical properties of the particulate matter

67 (Andreae and Rosenfeld, 2008). The physical state of PM, as liquid or non-liquid, can influence

68 the growth rates of small particles and ultimately the production of cloud condensation nuclei

69 (CCN) (Riipinen et al., 2011;Perraud et al., 2012). Liquid particles pose negligible in-particle

70 diffusion barriers for condensing species and therefore can grow rapidly. By comparison, non-

71 liquid particles, referring to both semisolid and solid particles, can have a different behavior. For

72 some conditions, semisolid particles can grow slowly because of in-particle limits on rates of

73 molecular diffusion, and solid particles can grow even more slowly when limited to surface

74 adsorption (Riipinen et al., 2012;Shiraiwa and Seinfeld, 2012;Li et al., 2015). Liquid compared

75 to non-liquid PM can also affect reactivity (Kuwata and Martin, 2012;Li et al., 2015). The

76 consequences of the differing growth mechanisms can be that the growth of small particles is

77 relatively disfavored in a population of liquid particles of heterogeneous sizes, as compared to a

78 similar population of non-liquid particles (Zaveri et al., 2014). An implication can be that CCN

79 concentrations are ultimately greater for a population of non-liquid particles that grows to CCN

80 sizes, as compared to a population of liquid particles.

81   Secondary organic material (SOM), produced by the oxidation of biogenic volatile

82 organic compounds (BVOCs), is a major source of atmospheric PM, especially over forested

83 regions where SOM often dominates the mass concentration of submicron PM (Hallquist et al.,

84 2009;Jimenez et al., 2009). The physical state of SOM has been studied in both laboratory

85 (Vaden et al., 2011;Kuwata and Martin, 2012;Perraud et al., 2012;Saukko et al., 2012;Renbaum-

Atmospheric
Chemistry
and Physics
Discussions

Open Access

86   Wolff et al., 2013;Kidd et al., 2014;Bateman et al., 2015;Li et al., 2015;Liu et al., 2015;Pajunoja

87   et al., 2015;Song et al., 2015) and ambient environments (Virtanen et al., 2010;O'Brien et al.,

88   2014;Bateman et al., 2016;Pajunoja et al., 2016). For background conditions of the Amazonian

89   tropical forest, a region dominated by isoprene-derived SOM and high RH, PM was mostly

90   liquid (Bateman et al., 2016). For a boreal forest in northern Europe, a region dominated by

91   pinene-derived SOM and low RH, PM was largely non-liquid (Virtanen et al., 2010). The

92   combined set of laboratory and ambient studies show that the physical state of PM having high

93   SOM content depends on the surrounding relative humidity (RH). This effect arises in part

94   because organic particles are hygroscopic to various extents depending on composition. Water

95   absorption, which is favored at elevated RH, has a plasticizing effect on physical state (Koop et

96   al., 2011).

97   The physical state of PM affected by urban pollution over forests remains largely

98   unexplored. A single day of ambient observations in central Amazonia suggested that ambient

99   PM affected by urban pollution tended toward a non-liquid state (Bateman et al., 2016), and

100   laboratory studies support the idea of an important modulating role of pollution in the physical

101   state of SOM. A non-liquid state was favored for SOM produced from single-ring aromatic

102   species (Liu et al., 2015;Song et al., 2015) as well as mixed with polycyclic aromatic

103   hydrocarbons (PAHs) (Zelenyuk et al., 2012;Abramson et al., 2013). Organic molecules

104   associated with urban pollution and industrial activities tend to be less hygroscopic than biogenic

105   SOM (Hersey et al., 2013). When internally mixed within biogenic SOM, the anthropogenic

106   molecules have a tendency to reduce water uptake and thereby reduce the viscosity of the mixed

107   particles. A similar line of reasoning leads to an identical hypothesis for the effects of biomass

108   burning emissions. Compared to prevailing background conditions of SOM dominance over

Atmospheric
Chemistry
and Physics
Discussions

109   many forests, PM produced by biomass burning leads to a net effect of decreased water uptake

110   when the PM mixes into the background particle population (Dusek et al., 2011).

111   The data sets presented herein provide observational evidence on the effects of

112   anthropogenic influences on the physical state of ambient particulate matter. All other factors

113   being equal, the lack of particle rebound is an indicator of liquid PM (Bateman et al., 2015).

114   Conversely, the occurrence of particle rebound is an indicator of non-liquid PM. Rebounding and

115   adhering particles were separately collected for conventional and chemical imaging. The data

116   sets were collected during the two Intensive Operating Periods (IOP1 and IOP2) of the

117   GoAmazon2014/5 experiment, corresponding to the wet and dry seasons, respectively (Martin et

118   al., 2016). The research site (-3.2133°, -60.5987°), called "T3", was located 70 km downwind of

119   the city of Manaus, population two million, in central Amazonia. Air masses representing

120   background conditions, urban pollution, and regional and continental scale biomass burning

121   passed over the research site. Herein, anthropogenic influence refers to all but background

122   conditions. Under background conditions, the submicron PM in this region is dominated by

123   biogenic SOM (Chen et al., 2009;Chen et al., 2015).

124   **2. Experimental**

125   An impactor apparatus was used for the study of particle rebound (Bateman et al.,

126   2014;Bateman et al., 2015;Bateman et al., 2016). The apparatus was housed inside a

127   temperature-controlled research trailer at the T3 site. Particulate matter was sampled at 5 m

128   above ground through copper tubing having an outer diameter of 13 mm (0.5 inch). In sequence,

129   a drying unit reduced the sampled flow to 25% RH or lower, a Differential Mobility Analyzer

130   (DMA, TSI 3085) selected a subpopulation of dried particles having a narrow distribution of

131   electric mobility, and a humidification unit (Nafion tubes; Perma Pure, MD 110) elevated the RH

Atmospheric
Chemistry
and Physics
Discussions

132   of the mobility-filtered flow to the targeted RH of a measurement. The drying unit consisted of a

133   Nafion drier in series with a silica gel diffusion drier, and the silica gel was replaced every two

134   days. After passing the dryer, DMA, and humidifier, the resulting flow was split and passed

135   through three impactors operated in parallel. Labels *i*, *ii*, and *iii* refer to each of the three

136   impactors. Each impactor was operated at a flow rate of 1.0 Lpm, corresponding to a setpoint

137   aerodynamic diameter d_a^* of 84.9 ± 5.4 nm (Bateman et al., 2014). Particle number

138   concentrations, denoted by N_i, N_{ii}, or N_{iii}, exiting the impactors were measured by three

139   independent condensation particle counters (CPC, TSI 3010). Measurements were conducted

140   from February 14 to March 16, 2014, during IOP1 and from September 4 to October 15, 2014,

141   during IOP2.

142   The three impactors differed from one another by having uncoated, coated, or no

143   impaction plate. The impactor having the uncoated plate passed both non-impacted and

144   rebounded particles. The impactor having the coated plate (Dow Corning High-Vacuum Grease)

145   passed only non-impacting particles. The impactor having no plate passed all particles. Its

146   purpose was to serve as a compensation arm for possible miscellaneous particle losses, such as

147   wall loss. Based on the particle number concentrations measured downstream of the impactors,

148   the rebound fraction was calculated as follows (Bateman et al., 2014):

149
$$f = \frac{N_i - N_{ii}}{N_{iii} - N_{ii}} \tag{1}$$

150   The terms N_i, N_{ii}, and N_{iii} represent the particle number concentration measured downstream of

151   the impactors having uncoated, coated, and no impaction plate, respectively. The standard

152   deviation of the rebound fraction was based on error propagation for an uncertainty in N of $N^{1/2}$

153   (Agarwal and Sem, 1980).

Atmospheric
Chemistry
and Physics
Discussions

154   A rebound curve representing f(RH) constituted an individual data set. For most

155   measurements, the DMA setting for electric mobility was held constant (typically 190 nm), the

156   RH in the humidification unit was changed stepwise every few minutes, and f was continuously

157   recorded. Additional protocols of DMA settings and RH profiles were used in a few cases. All

158   protocols, including differences between IOP1 and IOP2, are described in Section S1 of the

159   Supplement.

160   In conjunction with the rebound measurements, particles were collected for imaging by

161   transmission electron microscopy (TEM) and scanning transmission X-ray microscopy (STXM).

162   Images in some cases can directly suggest the liquid or non-liquid state of individual particles

163   (O'Brien et al., 2014;Wang et al., 2016). Samples for imaging were collected as follows. A fourth

164   impactor was added in parallel with the other three impactors. Imaging substrates were affixed to

165   the impaction plate, and multiple substrates were mounted to the plate for concurrent collection

166   for the various microscopy techniques. Substrates included grids coated with Formvar (EMJapan

167   Co., Tokyo, Japan) or lacey carbon (Ted Pella Inc., USA) for TEM and silicon nitride membrane

168   windows (Silson, UK) for STXM. The flow rate and setpoint aerodynamic diameter of the fourth

169   impactor were the same as for the other three impactors. The collected particles represented

170   those that adhered to the substrate at impact, and an assumption in the analysis is that rebound

171   from the substrate was similar to that from the uncoated plate. The flow through this fourth

172   impactor was pulled by an in-line TEM autosampler (Arios Inc., Tokyo, Japan (Adachi et al.,

173   2014)). In this way, the setup separately collected particles that adhered to the grids on the

174   impaction plate and particles that rebounded from the impaction plate and passed to the

175   autosampler. The autosampler collected particles having aerodynamic diameters from 60 to 350

176   nm. Particles adhered to the TEM substrates in the autosampler yet rebounded from the TEM

177   substrates in the impactor because of the significantly different particle impact velocities

178   between the two impactors (i.e., cut-point and impactor design). Samples were collected for

179   TEM analysis between September 30 and October 15, 2014. Samples were collected for STXM

180   analysis between 1:00 and 10:00 (UTC) on October 1, 2014.

181   Microanalysis of individual particles of the collected PM was performed using two

182   instruments: (1) a transmission electron microscope (TEM; JEOL, JEM-1400) equipped with an

183   energy-dispersive X-ray spectrometer (EDS; Oxford Instruments) and (2) a scanning

184   transmission X-ray microscope interfaced for near-edge X-ray absorption fine structure

185   spectroscopy (STXM/NEXAFS; Advanced Light Source, Berkeley). For TEM, imaging was by

186   bright-field microscopy, and particle composition was investigated by EDS. For STXM, at a

187   fixed photon energy an image was obtained by detecting the transmitted light at each pixel while

188   raster scanning the sample. Spatially resolved NEXAFS spectra were obtained from a set of

189   images recorded at different photon energies. The NEXAFS spectra provided chemical bonding

190   information and quantitative elemental ratios (Moffet et al., 2010a;Moffet et al., 2010b;O'Brien

191   et al., 2014;Piens et al., 2016). Section S2 of the Supplement presents further technical

192   information concerning the TEM and STXM/NEXAFS analyses.

193   Additional co-located measurements used in the data analysis herein included a High-

194   Resolution Time-of-Flight Aerosol Mass Spectrometer (AMS; Aerodyne Inc.) (Hu et al., 2015;de

195   Sá, 2016;Hu et al., 2016), a Single-Particle Soot Photometer (SP2; Droplet Measurement

196   Technologies), a size-resolved Cloud Condensation Nuclei Counter (CCNC; Droplet

197   Measurement Technologies, CCNC-100) (Thalman, 2016), a Condensation Particle Counter

198   (TSI, CPC 3772) for measuring particle number concentrations, an Integrated Cavity Output

199   Spectroscope (ICOS; Los Gatos) for measuring carbon monoxide (CO) concentration, and a

200   Trace Level Enhanced detector (TLE; Thermo Scientific, Model 42i, with further customization)

201   for the measuring concentrations of nitrogen oxides (NO_y). The latter three instruments were

202   deployed at the T3 site as part of the USA Department of Energy (DOE) Atmospheric Radiation

203   Measurement (ARM) Climate Research Facility, including the ARM Mobile Facility One (AMF-

204   1) and the Mobile Aerosol Observing System (MAOS) (Mather and Voyles, 2013;Martin et al.,

205   2016). This facility also collected the meteorological data used herein, including temperature,

206   relative humidity, wind direction, and wind speed. The AMS measured the chemical composition

207   in real-time of non-refractory submicron particles (DeCarlo et al., 2006). The high-resolution

208   data of the organic component in "V-mode" was used in conjunction with positive-matrix

209   factorization (PMF) analysis (Ulbrich et al., 2009) to obtain statistical factors and the associated

210   time series of factor loadings for each season (de Sá, 2016). As a surrogate for concentrations of

211   black carbon, the SP2 measured the time-resolved scattering and incandescence produced by

212   irradiated refractory, light-absorbing components of individual particles having volume-

213   equivalent diameters between 70 and 600 nm (Schwarz et al., 2006;Moteki and Kondo, 2007).

214   The size-resolved CCN activity was obtained by classifying dry particles using a DMA (TSI

215   3081) and then exposing them successively to a range of supersaturations inside the CCNC

216   (Thalman, 2016). The hygroscopicity and CCN activity were analyzed via κ-Köhler theory,

217   which relates particle critical supersaturation to the initial dry diameter and hygroscopicity

218   (Petters and Kreidenweis, 2007;Petters et al., 2009).

219   **3. Results and Discussion**

220   3.1 *Rebound Observations*

221   Particle rebound or particle adhesion at impact depends on the balance of energies.

222   Particle rebound occurs when the kinetic energy before impact is greater than the sum of

Atmospheric
Chemistry
and Physics
Discussions

223   dissipation and surface adhesion energies after impact (Tsai et al., 1990;Bateman et al., 2014).

224   The dissipation energy of liquid particles is much greater than that of solid particles because of

225   additional mechanisms of dissipation available to the former. Calibration of the impactor shows a

226   transition from rebound to adhesion between 10^2 to 1 Pa s in viscosity for sucrose particles

227   (Bateman et al., 2015).

228   The rebound curves of particles of 190-nm mobility diameter are shown in Figure 1a for

229   IOP1 and IOP2. For RH < 50%, the rebound fraction was between 0.8 and 1.0. For RH > 50%,

230   the rebound fraction decreased monotonically to a low value, typically zero. The shape of the

231   rebound curve in Figure 1a is similar to that for particles of secondary organic material produced

232   in the Harvard Environmental Chamber (Bateman et al., 2015). The rebound fraction of SOM

233   particles produced from isoprene or α-pinene became zero for RH > 90%.

234   The subset of the data for which the apparatus RH matched the ambient RH is shown in

235   Figure 1b (cf. Section S3 of Supplement). In light of the distribution of ambient RH values (cf.

236   Figure 1c), the data set in Figure 1b implies that submicron PM in this tropical environment was

237   liquid most of the time. Bateman et al. (2016) reported such a result for observations under

238   background conditions at this site for data sets collected in 2013 a few months before

239   GoAmazon2014/5 began. The present results reported for GoAmazon2014/5 represent a longer

240   time series (i.e., 550 compared to 30 rebound curves) and reinforce the generality of the earlier

241   result of Bateman et al. (2016) of the prevalence of liquid PM for this forested region under

242   background conditions.

243   In the larger set of observations of the present study, what also emerges is that the

244   rebound fraction remained in median at 0.05 even at 95% RH, implicating the presence of

245   externally mixed PM in the atmosphere. Approximately 5% of the particles were non-liquid even

Atmospheric
Chemistry
and Physics
Discussions

Open Access

EGU

246   to 95% RH in both the wet and dry seasons (i.e., IOP1 and IOP2) (Figures 1a and 1b). At times,

247   rebound fractions of up to 0.4 occurred for RH > 90%. Elevated rebound fractions were observed

248   more frequently in IOP2 than IOP1. During IOP2, which was extensively influenced by biomass

249   burning, non-liquid particles in median constituted a fraction of 0.3 at 70% RH and a fraction of

250   0.1 at 90%. These RH values prevailed approximately 10% of the time. Events of elevated

251   rebound fraction were associated with the pollution plume from Manaus during IOP1 in the wet

252   season and with both this urban plume as well as increased regional biomass burning during

253   IOP2 in the dry season (cf. Section 3.2).

254   Probability density functions (PDF) of rebound fraction at 75% RH based on the data

255   sets of Figure 1a are shown in Figure 2 for (a) IOP1 and (b) IOP2 for three types of air masses

256   during day and night time periods. Daytime represents 12:00 to 16:00 (local time) (16:00 to

257   20:00 UTC) and nighttime represents 23:00 to 04:00 (local time) (03:00 to 08:00 UTC). Air

258   masses were identified as background, as influenced by local to regional biomass burning, or as

259   influenced by Manaus pollution. The classification scheme was based on concentration regimes

260   of particle number, carbon monoxide, and odd nitrogen (NO_y), as presented in Section S4 of the

261   Supplement. Background conditions included contributions both from natural processes and

262   from the long-distance transport and extensive oxidation of biomass burning emissions (Chen et

263   al., 2009;Martin et al., 2010). Natural processes in this region were dominated by the production

264   of secondary organic material from oxidation of plant emissions (Martin et al., 2010;Poschl et

265   al., 2010). Figure 2a shows that the mode value of the PDF shifted higher under the influence of

266   Manaus pollution compared to background conditions, meaning that rebound became more

267   probable and indicating an increasing presence of non-liquid PM at 75% RH. In Figure 2b, the

268   mode value shifted even higher under the influence of biomass burning. For each type of air

Atmospheric
Chemistry
and Physics
Discussions

269   mass, the nighttime mode values were higher than the daytime equivalents. The day-night

270   differences were lowest under background conditions.

271   The increase in rebound at night might be explained by a combination of interacting

272   factors. A shallow stable nocturnal boundary layer can trap and thereby concentrate

273   anthropogenic non-liquid particles emitted at night from local emissions, including smoldering

274   fires during IOP2. During the day, the boundary layer expands and dilution is more effective. In

275   addition, the production of liquid secondary organic material by biogenic processes is

276   comparatively more rapid.

277   For further analysis, the rebound curves recorded under background conditions were

278   averaged separately for IOP1 and IOP2 (cf. Figure 1a and Section S5 of the Supplement). These

279   two background-average curves served as references against which deviations in rebound

280   fraction were calculated for all air masses. Rebound deviation represents the excess non-liquid

281   PM over background conditions after detrending the data for the dependence on relative

282   humidity. The rebound deviations for IOP1 and IOP2 are plotted in Figure 3. Rebound deviations

283   as high as +0.5 in rebound fraction were observed. Statistics of Figure 3 are summarized in Table

284   S1, including for the subset of measurements matched with the ambient RH. For the full set of

285   data, including the full range of RH, rebound deviations greater than 0.1 represented 17% and

286   35% of the observations during IOP1 and IOP2, respectively. These deviations, corresponding to

287   increased rebound and thus indicating an increasing presence of non-liquid PM, corresponded to

288   the anthropogenic influences, as developed further in Section 3.2.

Atmospheric
Chemistry
and Physics
Discussions

3.2 *Relationships between Rebound and Other Observations*

289

290   3.2.1 Case Studies

291   Transitions between background and polluted conditions across 24 hour-periods are

292   presented in Figure 4 as representative examples for each IOP. The bottom panel shows the

293   deviation in rebound fraction relative to the background-average curve (cf. Section S5 of

294   Supplement). Color coding distinguishes relative humidity. From bottom to top, other panels in

295   the figure show temperature, wind direction, wind speed, relative fractions of two groups of

296   AMS PMF factor loadings, black carbon (BC) concentration, sulfate concentration, and total

297   submicron PM mass concentration. Processes contributing to the loading of PMF group A are

298   largely associated with the background atmosphere of Amazonia, including the possibility of

299   long-range transport and extensive oxidation of biomass burning emissions. Processes

300   contributing to the loading of PMF group B are largely associated with urban pollution and local

301   and regional biomass burning (cf. Section S6 of Supplement).

302   Shifts in the deviation in the rebound fraction from the background-average curve are

303   apparent in the time series in the bottom panels of Figure 4. At these times, the fractional loading

304   of PMF group A decreased and that of PMF group B increased, indicating a shift away from

305   background conditions. Background conditions were characterized by high loadings of PMF

306   group A and small rebound deviations. In the left panel (IOP1), in an example of one type of an

307   anthropogenic event, black carbon concentration and the fractional loading of PMF group B

308   abruptly increased together. The rebound deviation simultaneously increased, indicating an

309   increasing presence of non-liquid PM, especially above 70% RH. In the right panel (IOP2), in an

310   example of a second type of an anthropogenic event, the background air mass was gently

311   replaced by an air mass characterized by small increases in rebound deviation and fractional

Atmospheric
Chemistry
and Physics
Discussions

Open Access

EGU

312   loading of PMF group B yet lacking an associated increase in black carbon concentration. In an

313   example of a third type of anthropogenic event, this air mass was later replaced by an air mass

314   characterized by a strong increase in the fractional loading of PMF group B, total PM mass

315   concentration, and rebound deviation. Around 15:00 (UTC), a convective event associated with

316   rainfall decreased temperature, changed wind direction, and increased wind velocity, and

317   background conditions returned.

318   TEM images collected during the time periods of elevated rebound corroborate the

319   foregoing interpretation of liquid and non-liquid PM for adhering compared to rebounding

320   particles. Images of particles that adhered to the TEM substrates in the impactor at 95% RH are

321   shown in Figure 5a. The images were taken at a tilt angle of 60° so that the aspect ratio of the

322   particles could be viewed. The images show that most adhering particles spread out across the

323   substrate, indicating flattening upon impact, as expected for liquid particles. Some of these

324   adhering particles had a mixed composition, appearing as solid cores surrounded by halos of

325   flattened liquid shells. The horizontal dimensions of the flattened particles approached 1 to 2 μm

326   for vertical dimensions of tens of nanometers. Pöschl et al. (2010) previously recorded similar

327   images for ambient particles in the wet season of 2008 in central Amazonia during the

328   Amazonian Characterization Experiment (AMAZE-08) (Martin et al., 2010). For comparison to

329   the images of the adhering particles, images of particles that rebounded at 95% RH from the

330   impaction plate are shown in Figure 5b. These particles were collected downstream of the

331   impactor. The images show that these particles had high vertical dimensions and spherical or

332   dome-like morphologies and thus suggest that the particles experienced little deformation upon

333   impact, as expected for solid particles.

Atmospheric
Chemistry
and Physics
Discussions

3.2.2 Descriptive Statistics

334

335   The results of Figures 3 and 4 are further analyzed in Figure 6. Statistics of rebound

336   deviation are shown by box-whisker representation for different windows of relative humidity.

337   The data sets were segregated for presentation by IOP1/IOP2, daytime/nighttime, and air mass

338   type. For background conditions, the rebound deviations relative to their average were mostly

339   zero, indicating that there was low variability among different background air masses. The

340   exception was for the night periods of IOP1. By comparison, under anthropogenic influences, the

341   rebound deviation was positive for both IOPs. Positive deviations were most significant between

342   65% and 95% RH. In all cases, the nighttime deviations were greater than the daytime

343   counterparts. For IOP2, the prevalence of biomass burning confounded separate classifications of

344   urban pollution and biomass burning, and a classification of biomass burning took precedent.

345   Rebound deviations were strongest during these time periods. Statistics of the analysis are further

346   summarized in Table S2 (cf. Section S7 of Supplement).

3.2.3 Statistical correlations

347

348   Scatter plots of rebound deviation with environmental variables of ambient temperature,

349   wind speed, and wind direction show no correlation for both daytime and nighttime datasets (cf.

350   Figure S1 of the Supplement). Scatter plots of rebound deviation with some possible

351   anthropogenic influences are presented in Figure S2. Soot, typically characterized by a solid core

352   region of black carbon, is expected in abundance both in urban pollution and biomass burning

353   emissions. There was, however, no correlation between rebound deviation and black carbon

354   concentrations. There was also no correlation between rebound deviation and total particle mass

355   concentration. Rebound deviation and sulfate concentration weakly anti-correlated, which might

356   be expected given the hygroscopicity of sulfate. Sulfate concentrations, however, were a poor

Atmospheric
Chemistry
and Physics
Discussions

357 indicator of anthropogenic influence in this region because the variability in background

358 concentrations was comparable in magnitude to any urban influence(de Sá, 2016). As a caveat,

359 an assumption in correlation tests is that variance arises from a single variable, and the

360 possibility of two or more contributing or interacting factors is not directly considered.

361   Given that water uptake is an important process for softening organic material, scatter

362 plots of the rebound deviation at 75% RH with the hygroscopicity parameter κ are shown in

363 Figures 7a and 7b for the data sets from IOP1 and IOP2, respectively. Lower values of κ

364 represent decreased equilibrium water uptake for a fixed RH (Petters and Kreidenweis, 2007).

365 The plots show that the rebound deviation increased as the κ value decreased, meaning that

366 particles of lower hygroscopicity were less prone to being in liquid form. The apparent shift to

367 higher κ values from IOP1 to IOP2 arose from instrumental methods. During IOP1, κ values

368 were measured using the impactor apparatus at sub-saturated RH (i.e., < 100%) (cf. Supplement

369 S8). During IOP2, κ values were measured using a size-resolved CCN instrument at super-

370 saturated RH (i.e., > 100%) (Thalman, 2016). In principle, the two kinds of κ values should have

371 similar numerical values for water-soluble species (Petters and Kreidenweis, 2007). The

372 observed shift is consistent with a more frequent occurrence of non-liquid particles during IOP2

373 (Pajunoja et al., 2015), in this case as a result of more extensive biomass burning, as well as the

374 possibility of liquid-liquid phase separation (Renbaum-Wolff et al., 2016).

375 3.2.4 Chemical characteristics of rebounded particles

376   An analysis of the relationship between rebound deviation and chemical characteristics is

377 presented in Figure 8 based on the fractional loading of PMF group B. The data sets are

378 segregated for presentation by IOP1/IOP2, daytime/nighttime, and four bands of fractional

379 loading. Within each panel, box-whisker statistics of rebound deviation are shown for different

Atmospheric
Chemistry
and Physics
Discussions

380   windows of relative humidity, ranging from 50% to 95%. The figure shows that the rebound

381   deviation increased at all RH values as the fractional loading of group B increased. The

382   background-average curve used as the reference for rebound deviation corresponded to a

383   fractional loading of 0.00 to 0.15 for group B or correspondingly of 0.85 to 1.00 for group A. An

384   increasing fractional loading of group B represented greater anthropogenic influence. The

385   inference is that anthropogenic influences, represented by a combination of urban pollution and

386   biomass burning, affected chemical composition in ways that increased the presence of non-

387   liquid PM above 50% RH.

388   Scatter plots between rebound deviation at 75% RH and the fractional loading of group B

389   are shown in Figures 9a and 9b for the data sets of the two IOPs. The data points are colored

390   according to the value of the hygroscopicity parameter κ. The plots show that rebound deviation

391   increased for low hygroscopicity and high fractional loading of group B, in agreement with the

392   presentation in Figures 7a and 7b and Figure 8. Figures 9a and 9b further show in explicit

393   fashion that the highest rebound deviations occurred during time periods affected by biomass

394   burning and urban pollution, as characterized by the lowest values of κ and the highest fractional

395   loadings of group B. Smaller κ values for lower fractional loadings of group B can be explained

396   by the differences in O:C ratios between group A and B (Massoli et al., 2010): the O:C ratios

397   were 0.95/0.95 (IOP1/IOP2) and 0.42/0.54 for groups A and B, respectively.

398   A model to predict rebound deviation based on chemical characteristics was constructed.

399   The fractional loadings of PMF group A and B were used as model inputs, and model

400   coefficients represented the effects of RH across nine bands (cf. Section S9 of the Supplement).

401   The observed and predicted rebound deviations are plotted in Figure 10. The corresponding

402   coefficients R^2 of determination were 0.65 and 0.72 for IOP1 and IOP2, respectively. Predicted

Atmospheric
Chemistry
and Physics

Discussions

Open Access

EGU

403   values were biased high for low rebound deviation and biased low for high rebound deviation.

404   The magnitudes of the model coefficients represented the relative importance of the two PMF

405   groups in predicting rebound deviation (Table S4). In this regard group B dominated during both

406   IOPs. This result is consistent with the role of anthropogenic influences in shifting the PM

407   population to fewer liquid particles and more non-liquid particles.

408   Analysis by STXM/NEXAFS supports the foregoing narrative of anthropogenic

409   influence as a modulator between liquid and non-liquid PM. Rebounded particles were collected

410   on October 1 during a time period classified as influenced by biomass burning emissions. The

411   carbon K-edge spectrum is shown in Figure 11a, and the STXM image is shown in Figure 11b. A

412   notable feature of the NEXAFS spectrum of the rebounded particles is the strong double bond.

413   Pöhlker et al. (2012) previously collected NEXAFS spectra for samples collected at a

414   background site in central Amazonia, and the strong feature of a double bond was absent. The

415   spectra instead resembled those of different types of reference biogenic secondary organic

416   material.

417   For comparison to the spectrum collected of the rebounded particles, carbon K-edge

418   spectra are shown for carbonaceous particles collected in other field and laboratory studies.

419   Based on these results as well as those of the rebound measurements, a hypothesis of soot or

420   black carbon to explain the rebounding particles was ruled out on three grounds. The double-

421   bond feature was homogeneously distributed throughout the particles (Figure 11b) compared to

422   inclusions that are typical for soot (Moffet et al., 2013;Knopf et al., 2014;O'Brien et al., 2014),

423   rebound deviation and black carbon concentrations did not correlate (Figure S2), and the

424   spectroscopic signatures of rebounded particles and soot did not match (Figure 11a). A

425   hypothesis of VOC-derived secondary organic material, including possible changes because of

Atmospheric
Chemistry
and Physics
Discussions

426   shifts from HO_2 to NO-dominant chemistry (Liu et al., 2016a;Liu et al., 2016b), was also

427   eliminated by comparison of the NEXAFS spectrum of the rebounded particles to the reference

428   spectra for laboratory samples. An important caveat to these interpretations is that some of the

429   hypotheses ruled out for this particular day might still have a role to play on other days.

430   There was exceptional uniformity in the particle population characterized by

431   STXM/NEXAFS, which could suggest that the rebounding PM represented distant sources or

432   alternatively a strong single nearby source. The gray region around the red line in Figure 11a

433   illustrates the low variability across the population of analyzed particles (Figure 11b). Moreover,

434   the variability in the O:C ratio determined by the NEXAFS analysis was just ± 0.01 for O:C =

435   0.34 (± 0.03) [± 0.01], where the value in parentheses was the uncertainty of the measurement

436   and the value in the bracket was the variability across the image in Figure 11b. During the same

437   time period, the O:C ratio of the ambient PM was 0.77 ± 0.04 by AMS measurements. Hence,

438   the rebounding particles were significantly less oxidized, as is consistent with lower

439   hygroscopicity, increased double bond (C=C) content, and increased fractional loading of PMF

440   group B.

441   Several speculations can be made for the origins of the particles leading to the data set of

442   October 1. The chemical constituents giving rise to the double bonds might derive from

443   biological degradation products from incomplete combustion, such as in biomass burning

444   (Tivanski et al., 2007;Keiluweit et al., 2010). Unexplained by this speculation, however, is the

445   absence of a potassium signature in the NEXAFS spectra, which is typical of most biomass

446   burning. Future collection of NEXAFS spectra would be well motivated for the several different

447   types of biomass burning in an Amazonian context, such as from nearby fields, regionally around

448   Manaus, two or three days away from other regions of South America, and up to a week away

Atmospheric
Chemistry
and Physics
Discussions

449   from Africa. An alternative speculation for this data set is that solid organic particles produced

450   by the impact of raindrops on wet soil surfaces could be making a contribution to the rebounded

451   PM analyzed here (Joung and Buie, 2015). Wang et al. (2016) recently reported detection of the

452   airborne soil organic particles generated by this mechanism over agricultural fields in the central

453   plains of the USA, and the corridor from Manaus to T3 has many agricultural fields. The

454   rebounded particles collected at T3 and the agricultural particles reported in Wang et al. (2016)

455   both had a homogeneous distribution of double bonds and similar elemental ratios and

456   absorption features. Even so, preliminary analysis across the extended data set at T3 between

457   rebound and nearby precipitation did not show a clear correlation. Another speculation relates to

458   the importance of aromatic compounds as hardening agents. Several gas-phase aromatic

459   compounds, laden with double bonds, were measured during IOP1 and IOP2, including toluene,

460   benzene, trimethylbenzene, and xylenes by proton-transfer mass spectrometry (Liu et al., 2016b).

461   Rebound deviation correlated positively with the concentrations of these compounds during both

462   IOPs, and the correlation was stronger during the night. Laboratory studies show that the uptake

463   of polycyclic aromatic hydrocarbons during the formation of biogenic PM can increase the

464   viscosity of the PM (Vaden et al., 2011;Zelenyuk et al., 2012;Abramson et al., 2013;Liu et al.,

465   2015).

466   **4. Conclusions**

467   Under background conditions, particles composed primarily of highly-oxidized biogenic

468   PM were hygroscopic, and they were liquid for the RH values prevailing over Amazonia at

469   surface level. Anthropogenic influences of urban pollution and biomass burning decreased

470   hygroscopicity, and non-liquid PM became more favored. The shift in physical state correlated

471   with decreasing values of the hygroscopicity parameter κ, decreasing O:C elemental ratios,

Atmospheric
Chemistry
and Physics
Discussions

Open Access

EGU

472   increasing concentrations of C=C functionalities, and increasing fractional loadings of AMS

473   PMF group B, all of which were indicative of anthropogenic influences. These results

474   demonstrate the importance of anthropogenic influences for altering the physical properties of

475   ambient particulate matter over tropical forests.

References

Abramson, E., Imre, D., Beranek, J., Wilson, J., and Zelenyuk, A.: Experimental determination of chemical diffusion within secondary organic aerosol particles, Phys. Chem. Chem. Phys., 15, 2983-2991, 10.1039/c2cp44013j, 2013.

Adachi, K., Zaizen, Y., Kajino, M., and Igarashi, Y.: Mixing state of regionally transported soot particles and the coating effect on their size and shape at a mountain site in japan, J. Geophys. Res. Atmos., 119, 5386-5396, 10.1002/2013jd020880, 2014.

Atmospheric
Chemistry
and Physics
Discussions

Open Access

Agarwal, J. K., and Sem, G. J.: Continuous-flow, single-particle-counting condensation nucleus counter, J. Aerosol Sci, 11, 343-&, 10.1016/0021-8502(80)90042-7, 1980.

Andreae, M. O., and Rosenfeld, D.: Aerosol-cloud-precipitation interactions. Part 1. The nature and sources of cloud-active aerosols, Earth Sci. Rev., 89, 13-41, 10.1016/j.earscirev.2008.03.001, 2008.

Bateman, A. P., Belassein, H., and Martin, S. T.: Impactor apparatus for the study of particle rebound: Relative humidity and capillary forces, Aerosol Sci. Technol., 48, 42-52, 10.1080/02786826.2013.853866, 2014.

Bateman, A. P., Bertram, A. K., and Martin, S. T.: Hygroscopic influence on the semisolid-to-liquid transition of secondary organic materials, J. Phys. Chem. A, 119, 4386-4395, 10.1021/jp508521c, 2015.

Bateman, A. P., Gong, Z., Liu, P., Sato, B., Cirino, G., Zhang, Y., Artaxo, P., Bertram, A. K., Manzi, A. O., Rizzo, L. V., Souza, R. A. F., Zaveri, R. A., and Martin, S. T.: Sub-micrometre particulate matter is primarily in liquid form over Amazon rainforest, Nature Geosci, 9, 34-37, 10.1038/ngeo2599, 2016.

Brechtel, F. J., and Kreidenweis, S. M.: Predicting particle critical supersaturation from hygroscopic growth measurements in the humidified TDMA. Part I: Theory and sensitivity studies, Journal of the Atmospheric Sciences, 57, 1854-1871, 10.1175/1520-0469(2000)057<1854:ppcsfh>2.0.co;2, 2000.

Chen, Q., Farmer, D. K., Schneider, J., Zorn, S. R., Heald, C. L., Karl, T. G., Guenther, A., Allan, J. D., Robinson, N., Coe, H., Kimmel, J. R., Pauliquevis, T., Borrmann, S., Poschl, U., Andreae, M. O., Artaxo, P., Jimenez, J. L., and Martin, S. T.: Mass spectral characterization of submicron biogenic organic particles in the Amazon basin, Geophys. Res. Lett., 36, L20806, 10.1029/2009gl039880, 2009.

Chen, Q., Farmer, D. K., Rizzo, L. V., Pauliquevis, T., Kuwata, M., Karl, T. G., Guenther, A., Allan, J. D., Coe, H., Andreae, M. O., Pöschl, U., Jimenez, J. L., Artaxo, P., and Martin, S. T.: Submicron particle mass concentrations and sources in the Amazonian wet season (AMAZE-08), Atmos. Chem. Phys., 15, 3687-3701, 10.5194/acp-15-3687-2015, 2015.

Cirino, G., Brito, J., Barbosa, H. M. J., Rizzo, L. V., Carbone, S., de Sa, S., Palm, B., Jimenez, J. L., Souza, R., Martin, S. T., and Artaxo, P.: Ground site observations of manaus plume evolution within the scope of GoAmazon2014/5, Atmospheric Chemisty and Physics, In Preparation, 2016.

de Sá, S. S.: In preparation, 2016.

DeCarlo, P. F., Kimmel, J. R., Trimborn, A., Northway, M. J., Jayne, J. T., Aiken, A. C., Gonin, M., Fuhrer, K., Horvath, T., Docherty, K. S., Worsnop, D. R., and Jimenez, J. L.: Field-deployable, high-resolution, time-of-flight aerosol mass spectrometer, Anal. Chem., 78, 8281-8289, 10.1021/ac061249n, 2006.

Atmospheric
Chemistry
and Physics
Discussions

Open Access

Dusek, U., Frank, G. P., Massling, A., Zeromskiene, K., Iinuma, Y., Schmid, O., Helas, G., Hennig, T., Wiedensohler, A., and Andreae, M. O.: Water uptake by biomass burning aerosol at sub- and supersaturated conditions: Closure studies and implications for the role of organics, Atmos. Chem. Phys., 11, 9519-9532, 10.5194/acp-11-9519-2011, 2011.

Hallquist, M., Wenger, J. C., Baltensperger, U., Rudich, Y., Simpson, D., Claeys, M., Dommen, J., Donahue, N. M., George, C., Goldstein, A. H., Hamilton, J. F., Herrmann, H., Hoffmann, T., Iinuma, Y., Jang, M., Jenkin, M. E., Jimenez, J. L., Kiendler-Scharr, A., Maenhaut, W., McFiggans, G., Mentel, T. F., Monod, A., Prevot, A. S. H., Seinfeld, J. H., Surratt, J. D., Szmigielski, R., and Wildt, J.: The formation, properties and impact of secondary organic aerosol: Current and emerging issues, Atmos. Chem. Phys., 9, 5155-5236, 10.5194/acp-9-5155-2009, 2009.

Hersey, S. P., Craven, J. S., Metcalf, A. R., Lin, J., Lathem, T., Suski, K. J., Cahill, J. F., Duong, H. T., Sorooshian, A., Jonsson, H. H., Shiraiwa, M., Zuend, A., Nenes, A., Prather, K. A., Flagan, R. C., and Seinfeld, J. H.: Composition and hygroscopicity of the los angeles aerosol: Calnex, Journal of Geophysical Research: Atmospheres, 118, 3016-3036, 10.1002/jgrd.50307, 2013.

Hu, W., Palm, B. B., Day, D. A., Campuzano-Jost, P., Krechmer, J. E., Peng, Z., de Sá, S. S., Martin, S. T., Alexander, M. L., Baumann, K., Hacker, L., Kiendler-Scharr, A., Koss, A. R., de Gouw, J. A., Goldstein, A. H., Seco, R., Sjostedt, S. J., Park, J. H., Guenther, A. B., Kim, S., Canonaco, F., Prévôt, Brune, W. H., and Jimenez, J. L.: Volatility and lifetime against OH heterogeneous reaction of ambient isoprene epoxydiols-derived secondary organic aerosol (IEPOX-SOA), Atmos. Chem. Phys. Discuss., 2016, 1-35, 10.5194/acp-2016-418, 2016.

Hu, W. W., Campuzano-Jost, P., Palm, B. B., Day, D. A., Ortega, A. M., Hayes, P. L., Krechmer, J. E., Chen, Q., Kuwata, M., Liu, Y. J., de Sá, S. S., McKinney, K., Martin, S. T., Hu, M., Budisulistiorini, S. H., Riva, M., Surratt, J. D., St. Clair, J. M., Isaacman-Van Wertz, G., Yee, L. D., Goldstein, A. H., Carbone, S., Brito, J., Artaxo, P., de Gouw, J. A., Koss, A., Wisthaler, A., Mikoviny, T., Karl, T., Kaser, L., Jud, W., Hansel, A., Docherty, K. S., Alexander, M. L., Robinson, N. H., Coe, H., Allan, J. D., Canagaratna, M. R., Paulot, F., and Jimenez, J. L.: Characterization of a real-time tracer for isoprene epoxydiols-derived secondary organic aerosol (IEPOX-SOA) from aerosol mass spectrometer measurements, Atmos. Chem. Phys., 15, 11807-11833, 10.5194/acp-15-11807-2015, 2015.

Jimenez, J. L., Canagaratna, M. R., Donahue, N. M., Prevot, A. S. H., Zhang, Q., Kroll, J. H., DeCarlo, P. F., Allan, J. D., Coe, H., Ng, N. L., Aiken, A. C., Docherty, K. S., Ulbrich, I. M., Grieshop, A. P., Robinson, A. L., Duplissy, J., Smith, J. D., Wilson, K. R., Lanz, V. A., Hueglin, C., Sun, Y. L., Tian, J., Laaksonen, A., Raatikainen, T., Rautiainen, J., Vaattovaara, P., Ehn, M., Kulmala, M., Tomlinson, J. M., Collins, D. R., Cubison, M. J., Dunlea, E. J., Huffman, J. A., Onasch, T. B., Alfarra, M. R., Williams, P. I., Bower, K., Kondo, Y., Schneider, J., Drewnick, F., Borrmann, S., Weimer, S., Demerjian, K., Salcedo, D., Cottrell, L., Griffin, R., Takami, A., Miyoshi, T., Hatakeyama, S., Shimono, A., Sun, J. Y., Zhang, Y. M., Dzepina, K., Kimmel, J. R., Sueper, D., Jayne, J. T., Herndon, S. C., Trimborn, A. M., Williams, L. R., Wood, E. C., Middlebrook, A. M., Kolb, C. E., Baltensperger, U., and Worsnop, D. R.: Evolution of organic aerosols in the atmosphere, Science, 326, 1525-1529, 10.1126/science.1180353, 2009.

Atmospheric
Chemistry
and Physics

Open Access

EGU

Discussions

Joung, Y. S., and Buie, C. R.: Aerosol generation by raindrop impact on soil, Nature Communications, 6, 10.1038/ncomms7083, 2015.

Keiluweit, M., Nico, P. S., Johnson, M. G., and Kleber, M.: Dynamic molecular structure of plant biomass-derived black carbon (biochar), Environ. Sci. Technol., 44, 1247-1253, 10.1021/es9031419, 2010.

Kelly, W. P., and McMurry, P. H.: Measurement of particle density by inertial classification of differential mobility analyzer generated monodisperse aerosols, Aerosol Sci. Technol., 17, 199-212, 10.1080/02786829208959571, 1992.

Kidd, C., Perraud, V., Wingen, L. M., and Finlayson-Pitts, B. J.: Integrating phase and composition of secondary organic aerosol from the ozonolysis of α-pinene, Proc. Natl. Acad. Sci. U. S. A., 111, 7552-7557, 10.1073/pnas.1322558111, 2014.

Knopf, D. A., Alpert, P. A., Wang, B., O'Brien, R. E., Kelly, S. T., Laskin, A., Gilles, M. K., and Moffet, R. C.: Microspectroscopic imaging and characterization of individually identified ice nucleating particles from a case field study, J. Geophys. Res. Atmos., 119, 10.1002/2014jd021866, 2014.

Koop, T., Bookhold, J., Shiraiwa, M., and Poschl, U.: Glass transition and phase state of organic compounds: Dependency on molecular properties and implications for secondary organic aerosols in the atmosphere, Phys. Chem. Chem. Phys., 13, 19238-19255, 10.1039/c1cp22617g, 2011.

Kuwata, M., and Martin, S. T.: Phase of atmospheric secondary organic material affects its reactivity, Proc. Natl. Acad. Sci. U. S. A., 109, 17354-17359, 10.1073/pnas.1209071109, 2012.

Li, Y. J., Liu, P. F., Gong, Z. H., Wang, Y., Bateman, A. P., Bergoend, C., Bertram, A. K., and Martin, S. T.: Chemical reactivity and liquid/nonliquid states of secondary organic material, Environ. Sci. Technol., 49, 13264-13274, 10.1021/acs.est.5b03392, 2015.

Liu, P., Li, Y., Wang, Y., Gilles, M. K., Zaveri, R. A., Bertram, A. K., and Martin, S. T.: Lability of atmospheric organic particulate matter, Submitted, 2016a.

Liu, P. F., Abdelmalki, N., Hung, H. M., Wang, Y., Brune, W. H., and Martin, S. T.: Ultraviolet and visible complex refractive indices of secondary organic material produced by photooxidation of the aromatic compounds toluene and m-xylene, Atmos. Chem. Phys., 15, 1435-1446, 10.5194/acp-15-1435-2015, 2015.

Liu, Y., Brito, J., Dorris, M. R., Rivera-Rios, J. C., Seco, R., Bates, K. H., Artaxo, P., Duvoisin, S., Keutsch, F. N., Kim, S., Goldstein, A. H., Guenther, A. B., Manzi, A. O., Souza, R. A. F., Springston, S. R., Watson, T. B., McKinney, K. A., and Martin, S. T.: Isoprene photochemistry over the Amazon rainforest, Proc. Natl. Acad. Sci. U. S. A., 113, 6125-6130, 10.1073/pnas.1524136113, 2016b.

Martin, S. T., Andreae, M. O., Althausen, D., Artaxo, P., Baars, H., Borrmann, S., Chen, Q., Farmer, D. K., Guenther, A., Gunthe, S. S., Jimenez, J. L., Karl, T., Longo, K., Manzi, A.,

Atmospheric
Chemistry
and Physics
Discussions

Muller, T., Pauliquevis, T., Petters, M. D., Prenni, A. J., Poschl, U., Rizzo, L. V., Schneider, J., Smith, J. N., Swietlicki, E., Tota, J., Wang, J., Wiedensohler, A., and Zorn, S. R.: An overview of the Amazonian aerosol characterization experiment 2008 (AMAZE-08), Atmos. Chem. Phys., 10, 11415-11438, 10.5194/acp-10-11415-2010, 2010.

Martin, S. T., Artaxo, P., Machado, L. A. T., Manzi, A. O., Souza, R. A. F., Schumacher, C., Wang, J., Andreae, M. O., Barbosa, H. M. J., Fan, J., Fisch, G., Goldstein, A. H., Guenther, A., Jimenez, J. L., Pöschl, U., Silva Dias, M. A., Smith, J. N., and Wendisch, M.: Introduction: Observations and modeling of the green ocean Amazon (GoAmazon2014/5), Atmos. Chem. Phys., 16, 4785-4797, 10.5194/acp-16-4785-2016, 2016.

Massoli, P., Lambe, A. T., Ahern, A. T., Williams, L. R., Ehn, M., Mikkila, J., Canagaratna, M. R., Brune, W. H., Onasch, T. B., Jayne, J. T., Petaja, T., Kulmala, M., Laaksonen, A., Kolb, C. E., Davidovits, P., and Worsnop, D. R.: Relationship between aerosol oxidation level and hygroscopic properties of laboratory generated secondary organic aerosol (SOA) particles, Geophys. Res. Lett., 37, L24801, 10.1029/2010gl045258, 2010.

Mather, J. H., and Voyles, J. W.: The arm climate research facility: A review of structure and capabilities, Bulletin of the American Meteorological Society, 94, 377-392, doi:10.1175/BAMS-D-11-00218.1, 2013.

Moffet, R. C., Henn, T., Laskin, A., and Gilles, M. K.: Automated chemical analysis of internally mixed aerosol particles using X-ray spectromicroscopy at the carbon K-edge, Anal. Chem., 82, 7906-7914, 10.1021/ac1012909, 2010a.

Moffet, R. C., Tivanski, A. V., and Gilles, M. K.: Scanning transmission X-ray microscopy, in: Fundamentals and applications in aerosol spectroscopy, CRC Press, 419-462, 2010b.

Moffet, R. C., Rodel, T. C., Kelly, S. T., Yu, X. Y., Carroll, G. T., Fast, J., Zaveri, R. A., Laskin, A., and Gilles, M. K.: Spectro-microscopic measurements of carbonaceous aerosol aging in central california, Atmos. Chem. Phys., 13, 10445-10459, 10.5194/acp-13-10445-2013, 2013.

Moteki, N., and Kondo, Y.: Effects of mixing state on black carbon measurements by laser-induced incandescence, Aerosol Sci. Technol., 41, 398-417, 10.1080/02786820701199728, 2007.

O'Brien, R. E., Neu, A., Epstein, S. A., MacMillan, A. C., Wang, B. B., Kelly, S. T., Nizkorodov, S. A., Laskin, A., Moffet, R. C., and Gilles, M. K.: Physical properties of ambient and laboratory-generated secondary organic aerosol, Geophys. Res. Lett., 41, 4347-4353, 10.1002/2014gl060219, 2014.

Pajunoja, A., Lambe, A. T., Hakala, J., Rastak, N., Cummings, M. J., Brogan, J. F., Hao, L., Paramonov, M., Hong, J., Prisle, N. L., Malila, J., Romakkaniemi, S., Lehtinen, K. E. J., Laaksonen, A., Kulmala, M., Massoli, P., Onasch, T. B., Donahue, N. M., Riipinen, I., Davidovits, P., Worsnop, D. R., Petäjä, T., and Virtanen, A.: Adsorptive uptake of water by semisolid secondary organic aerosols, Geophys. Res. Lett., 42, 3063-3068, 10.1002/2015gl063142, 2015.

Pajunoja, A., Hu, W., Leong, Y. J., Taylor, N. F., Miettinen, P., Palm, B. B., Mikkonen, S., Collins, D. R., Jimenez, J. L., and Virtanen, A.: Phase state of ambient aerosol linked with water uptake and chemical aging in the southeastern us, Atmos. Chem. Phys. Discuss., 2016, 1-25, 10.5194/acp-2016-375, 2016.

Perraud, V., Bruns, E. A., Ezell, M. J., Johnson, S. N., Yu, Y., Alexander, M. L., Zelenyuk, A., Imre, D., Chang, W. L., Dabdub, D., Pankow, J. F., and Finlayson-Pitts, B. J.: Nonequilibrium atmospheric secondary organic aerosol formation and growth, Proc. Natl. Acad. Sci. U. S. A., 109, 2836-2841, 10.1073/pnas.1119909109, 2012.

Petters, M. D., and Kreidenweis, S. M.: A single parameter representation of hygroscopic growth and cloud condensation nucleus activity, Atmos. Chem. Phys., 7, 1961-1971, 10.5194/acp-7-1961-2007, 2007.

Petters, M. D., Carrico, C. M., Kreidenweis, S. M., Prenni, A. J., DeMott, P. J., Collett, J. L., and Moosmuller, H.: Cloud condensation nucleation activity of biomass burning aerosol, J. Geophys. Res. Atmos., 114, D22205, 10.1029/2009jd012353, 2009.

Piens, D. S., Kelly, S. T., Harder, T. H., Petters, M. D., O'Brien, R. E., Wang, B., Teske, K., Dowell, P., Laskin, A., and Gilles, M. K.: Measuring mass-based hygroscopicity of atmospheric particles through in situ imaging, Environ. Sci. Technol., 50, 5172-5180, 10.1021/acs.est.6b00793, 2016.

Pohlker, C., Wiedemann, K. T., Sinha, B., Shiraiwa, M., Gunthe, S. S., Smith, M., Su, H., Artaxo, P., Chen, Q., Cheng, Y. F., Elbert, W., Gilles, M. K., Kilcoyne, A. L. D., Moffet, R. C., Weigand, M., Martin, S. T., Poeschl, U., and Andreae, M. O.: Biogenic potassium salt particles as seeds for secondary organic aerosol in the Amazon, Science, 337, 1075-1078, 10.1126/science.1223264, 2012.

Poschl, U., Martin, S. T., Sinha, B., Chen, Q., Gunthe, S. S., Huffman, J. A., Borrmann, S., Farmer, D. K., Garland, R. M., Helas, G., Jimenez, J. L., King, S. M., Manzi, A., Mikhailov, E., Pauliquevis, T., Petters, M. D., Prenni, A. J., Roldin, P., Rose, D., Schneider, J., Su, H., Zorn, S. R., Artaxo, P., and Andreae, M. O.: Rainforest aerosols as biogenic nuclei of clouds and precipitation in the Amazon, Science, 329, 1513-1516, 10.1126/science.1191056, 2010.

Ramanathan, V., Crutzen, P. J., Kiehl, J. T., and Rosenfeld, D.: Atmosphere - aerosols, climate, and the hydrological cycle, Science, 294, 2119-2124, 10.1126/science.1064034, 2001.

Renbaum-Wolff, L., Grayson, J. W., Bateman, A. P., Kuwata, M., Sellier, M., Murray, B. J., Shilling, J. E., Martin, S. T., and Bertram, A. K.: Viscosity of α-pinene secondary organic material and implications for particle growth and reactivity, Proc. Natl. Acad. Sci. U. S. A., 10.1073/pnas.1219548110, 2013.

Renbaum-Wolff, L., Song, M., Marcolli, C., Zhang, Y., Liu, P. F., Grayson, J. W., Geiger, F. M., Martin, S. T., and Bertram, A. K.: Observations and implications of liquid–liquid phase separation at high relative humidities in secondary organic material produced by α-pinene ozonolysis without inorganic salts, Atmos. Chem. Phys., 16, 7969-7979, 10.5194/acp-16-7969-2016, 2016.

Riipinen, I., Pierce, J. R., Yli-Juuti, T., Nieminen, T., Hakkinen, S., Ehn, M., Junninen, H., Lehtipalo, K., Petaja, T., Slowik, J., Chang, R., Shantz, N. C., Abbatt, J., Leaitch, W. R., Kerminen, V. M., Worsnop, D. R., Pandis, S. N., Donahue, N. M., and Kulmala, M.: Organic condensation: A vital link connecting aerosol formation to cloud condensation nuclei (CCN) concentrations, Atmos. Chem. Phys., 11, 3865-3878, 10.5194/acp-11-3865-2011, 2011.

Riipinen, I., Yli-Juuti, T., Pierce, J. R., Petaja, T., Worsnop, D. R., Kulmala, M., and Donahue, N. M.: The contribution of organics to atmospheric nanoparticle growth, Nature Geosci., 5, 453-458, 10.1038/ngeo1499, 2012.

Saukko, E., Lambe, A. T., Massoli, P., Koop, T., Wright, J. P., Croasdale, D. R., Pedernera, D. A., Onasch, T. B., Laaksonen, A., Davidovits, P., Worsnop, D. R., and Virtanen, A.: Humidity-dependent phase state of SOA particles from biogenic and anthropogenic precursors, Atmos. Chem. Phys., 12, 7517-7529, 10.5194/acp-12-7517-2012, 2012.

Schwarz, J. P., Gao, R. S., Fahey, D. W., Thomson, D. S., Watts, L. A., Wilson, J. C., Reeves, J. M., Darbeheshti, M., Baumgardner, D. G., Kok, G. L., Chung, S. H., Schulz, M., Hendricks, J., Lauer, A., Karcher, B., Slowik, J. G., Rosenlof, K. H., Thompson, T. L., Langford, A. O., Loewenstein, M., and Aikin, K. C.: Single-particle measurements of midlatitude black carbon and light-scattering aerosols from the boundary layer to the lower stratosphere, J. Geophys. Res. Atmos., 111, D16207, 10.1029/2006jd007076, 2006.

Shiraiwa, M., and Seinfeld, J. H.: Equilibration timescale of atmospheric secondary organic aerosol partitioning, Geophys. Res. Lett., 39, 10.1029/2012gl054008, 2012.

Song, M., Liu, P. F., Hanna, S. J., Li, Y. J., Martin, S. T., and Bertram, A. K.: Relative humidity-dependent viscosities of isoprene-derived secondary organic material and atmospheric implications for isoprene-dominant forests, Atmos. Chem. Phys., 15, 5145-5159, 10.5194/acp-15-5145-2015, 2015.

Thalman, R.: In preparation, 2016.

Tivanski, A. V., Hopkins, R. J., Tyliszczak, T., and Gilles, M. K.: Oxygenated interface on biomass burn tar balls determined by single particle scanning transmission X-ray microscopy, J. Phys. Chem. A, 111, 5448-5458, 10.1021/jp070155u, 2007.

Tsai, C. J., Pui, D. Y. H., and Liu, B. Y. H.: Capture and rebound of small particles upon impact with solid-surfaces, Aerosol Sci. Technol., 12, 497-507, 10.1080/02786829008959364, 1990.

Ulbrich, I. M., Canagaratna, M. R., Zhang, Q., Worsnop, D. R., and Jimenez, J. L.: Interpretation of organic components from positive matrix factorization of aerosol mass spectrometric data, Atmos. Chem. Phys., 9, 2891-2918, 10.5194/acp-9-2891-2009, 2009.

Vaden, T. D., Imre, D., Beranek, J., Shrivastava, M., and Zelenyuk, A.: Evaporation kinetics and phase of laboratory and ambient secondary organic aerosol, Proc. Natl. Acad. Sci. U. S. A., 108, 2190-2195, 10.1073/pnas.1013391108, 2011.

Virtanen, A., Joutsensaari, J., Koop, T., Kannosto, J., Yli-Pirila, P., Leskinen, J., Makela, J. M., Holopainen, J. K., Poschl, U., Kulmala, M., Worsnop, D. R., and Laaksonen, A.: An amorphous solid state of biogenic secondary organic aerosol particles, Nature, 467, 824-827, 10.1038/nature09455, 2010.

Wang, B., Harder, T. H., Kelly, S. T., Piens, D. S., China, S., Kovarik, L., Keiluweit, M., Arey, B. W., Gilles, M. K., and Laskin, A.: Airborne soil organic particles generated by precipitation, Nature Geosci, 9, 433-437, 10.1038/ngeo2705, 2016.

Zaveri, R. A., Easter, R. C., Shilling, J. E., and Seinfeld, J. H.: Modeling kinetic partitioning of secondary organic aerosol and size distribution dynamics: Representing effects of volatility, phase state, and particle-phase reaction, Atmos. Chem. Phys., 14, 5153-5181, 10.5194/acp-14-5153-2014, 2014.

Zelenyuk, A., Imre, D., Beranek, J., Abramson, E., Wilson, J., and Shrivastava, M.: Synergy between secondary organic aerosols and long-range transport of polycyclic aromatic hydrocarbons, Environ. Sci. Technol., 46, 12459-12466, 10.1021/es302743z, 2012.

Atmospheric
Chemistry
and Physics

Open Access

EGU

Discussions

Figure Captions

Figure 1.   Rebound fraction as a function of apparatus relative humidity during IOP1 (blue)
and IOP2 (red), corresponding respectively to the wet and dry seasons in central
Amazonia. Panel (a) shows all measurements. Panel (b) shows the subset of data for
which the apparatus RH matched the ambient relative humidity (cf. Supplement
S3). Panel (c) represents the probability density function of relative humidity at the
T3 site during the wet and dry seasons of 2014. Points represent rebound
measurements for particles having mobility diameters of 190 nm. Statistics of
measurements group by relative humidity are represented in box-whisker format.
The horizontal line within a box indicates the median of the points, the horizontal
lines at the box boundaries indicate quartiles, and horizontal lines most distant from
the box indicate 10% and 90% quantiles. For comparison, the black line shows the
rebound curve for particles of secondary organic material produced by
photooxidation of an isoprene/α-pinene mixture in the Harvard Environmental
Chamber (Bateman et al., 2015).

Figure 2.   Probability density function of rebound fraction during (a) IOP1 and (b) IOP2 for
categorization by type of air mass and time of day: background conditions (green),
Manaus pollution (red), and biomass burning (orange). Solid and dashed lines
respectively represent daytime (12:00 to 16:00, local time; 16:00 to 20:00, UTC)
and nighttime measurements (23:00 to 04:00, local time; 03:00 to 08:00 UTC).
Results are shown for an apparatus RH of 75% and for particles having a mobility
diameter of 190 nm.

Atmospheric
Chemistry
and Physics
Discussions

Figure 3. Deviation in rebound fraction relative to the average curve for background conditions during (a) IOP1 and (b) IOP2. Red, purple, and green coloring correspond respectively to the RH regions of rebound, transition, and adhesion for the background-average curve. Results are shown for particles having a mobility diameter of 190 nm.

Figure 4. Time series of representative species during two pollution events for IOP1 and IOP2 (left and right sides of figures, respectively). "Total mass concentration" plotted in the figure represents the sum of the AMS and black carbon mass concentrations measured for submicron PM. The PMF mass fractions are expressed in relative terms to one another and necessarily sum to unity. Time on the abscissa is expressed in UTC.

Figure 5. Representative TEM images of (a) adhering and (b) rebounding PM at 95% RH collected between 14:15 and 18:15 (UTC) on September 30, 2014, during IOP2. The rebound fraction during the time period of collection approached 0.3. The arrows in panel (b) highlight the locations of particles having high vertical dimensions and spherical or dome-like morphologies, as expected for solid particles.

Figure 6. Deviation in rebound fraction for categorization by type of air mass and time of day. The box-whisker representation of the 10%, 25%, 50%, 75%, and 90% quantiles of statistics for each RH bin is explained in the caption to Figure 1. Air mass categorization is as for Figure 2. Results are shown for particles having a mobility diameter of 190 nm.

Figure 7. Scatter plot of rebound deviation with the hygroscopicity parameter κ for (a) IOP1 and (b) IOP2. For clarity of presentation, data points are shown for apparatus RH values between 73 and 78%, although the trend applies more broadly. As a guide to the eye, in each panel data are divided into four groups, and medians and quartiles of the groups are plotted as black circles and whiskers, respectively.

Figure 8. Deviation in rebound fraction for categorization by chemical characteristics. The box-whisker representation of the 10%, 25%, 50%, 75%, and 90% quantiles of rebound fraction is explained in the caption to Figure 1. The chemical characteristics are categorized by the fractional loading of PMF group B as < 0.15 (green), 0.15 to 0.3 (blue), 0.3 to 0.6 (orange), and > 0.6 (red).

Figure 9. Scatter plot of rebound deviation with the fractional loading of PMF group B for (a) IOP1 and (b) IOP2. The data points are colored according to the corresponding hygroscopicity parameter κ. For clarity of presentation, data points are shown for apparatus RH values between 73 and 78%, although the trend applies more broadly. As a guide to the eye, in each panel data are divided into four groups, and medians and quartiles of the groups are plotted as black circles and whiskers, respectively.

Figure 10. Scatter plot of observed compared to predicted rebound deviation for (a) IOP1 and (b) IOP2. Predictions are based on linear combinations of the loadings of the two PMF groups. The linear coefficients used in the prediction were optimized as a function of RH (Table S4). The solid line represents a one-to-one correlation, and the dashed line represents the best linear fit. Coefficients R^2 of determination were 0.65 and 0.72 for the IOP1 and IOP2 datasets, respectively. Points are color-coded by relative humidity.

Figure 11. STXM/NEXAFS analysis of particles collected after rebound from the impaction plate. Samples were collected between 1:00 and 10:00 (UTC) of October 1, 2014. (a) Carbon K-edge spectrum of rebounded particles (red). Lines at 285.4 and 288.5 eV highlight absorption by double bonds (C=C) and carboxylic acids (-COOH), respectively. The line in the region of 286.5 to 286.7 eV can have contributions from ketones, carbonyl-substituted aromatics, and phenolic species. For comparison, spectra are shown for carbonaceous particles collected in other field and laboratory studies: soil organic particles from central USA (Wang et al., 2016), soot from the ambient environment, atmospheric particles collected at a background site in central Amazonia (Pohlker et al., 2012), and three laboratory samples of secondary organic material. Data sources: isoprene-derived SOM produced under HO_2-dominant conditions (O'Brien et al., 2014); isoprene-derived SOM produced under NO-dominant conditions (O'Brien et al., 2014), and toluene-derived SOM produced under NO-dominant conditions (this study). (b) STXM image from which the NEXAFS spectrum of panel (a) was obtained. Coloring is by red for absorption at 285.4 eV (i.e., double bonds). Coloring is by green for other types of functionalities. The pixelation visible in the image corresponds to the STXM spatial resolution during data collection.
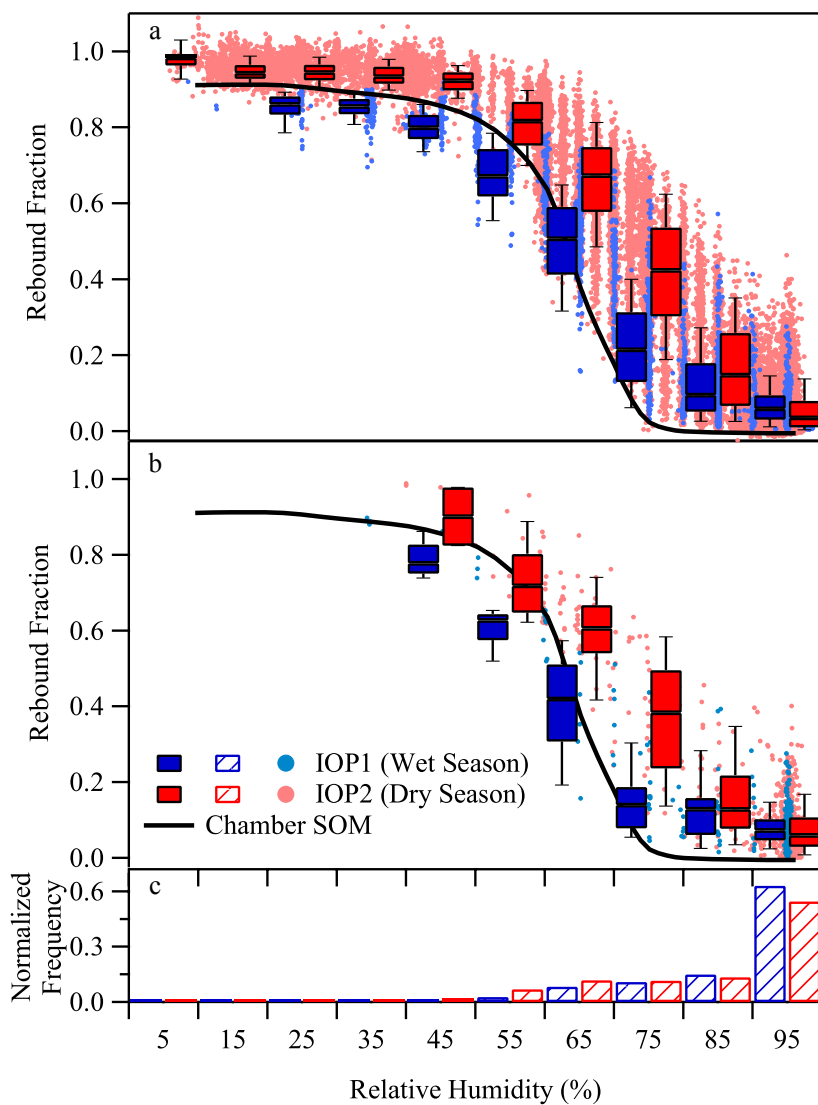
Figure 1
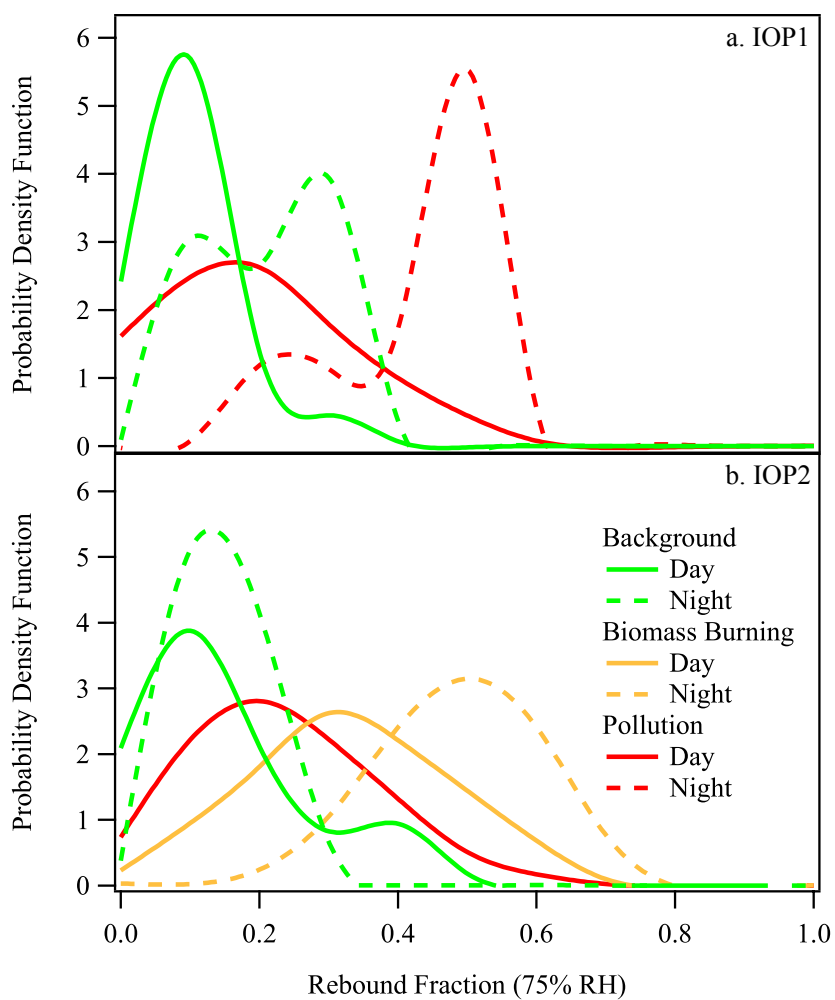
Figure 2

Figure 3

Figure 4

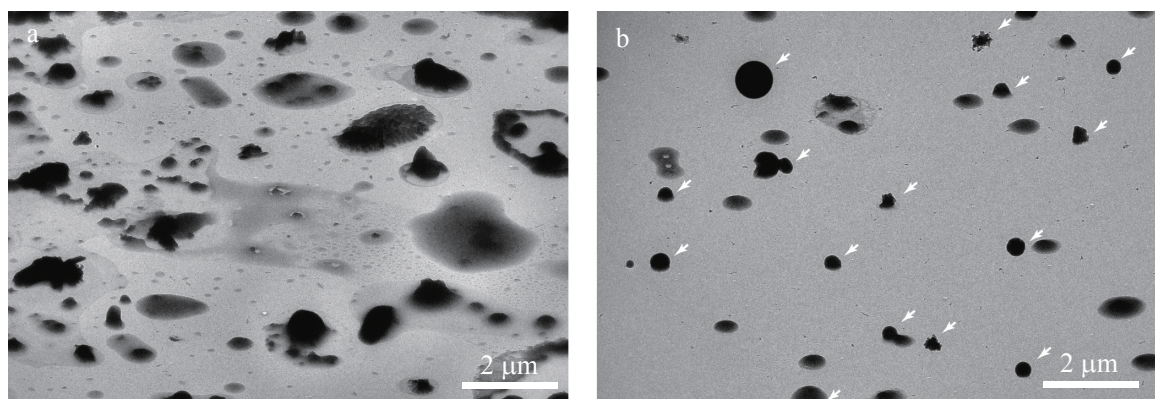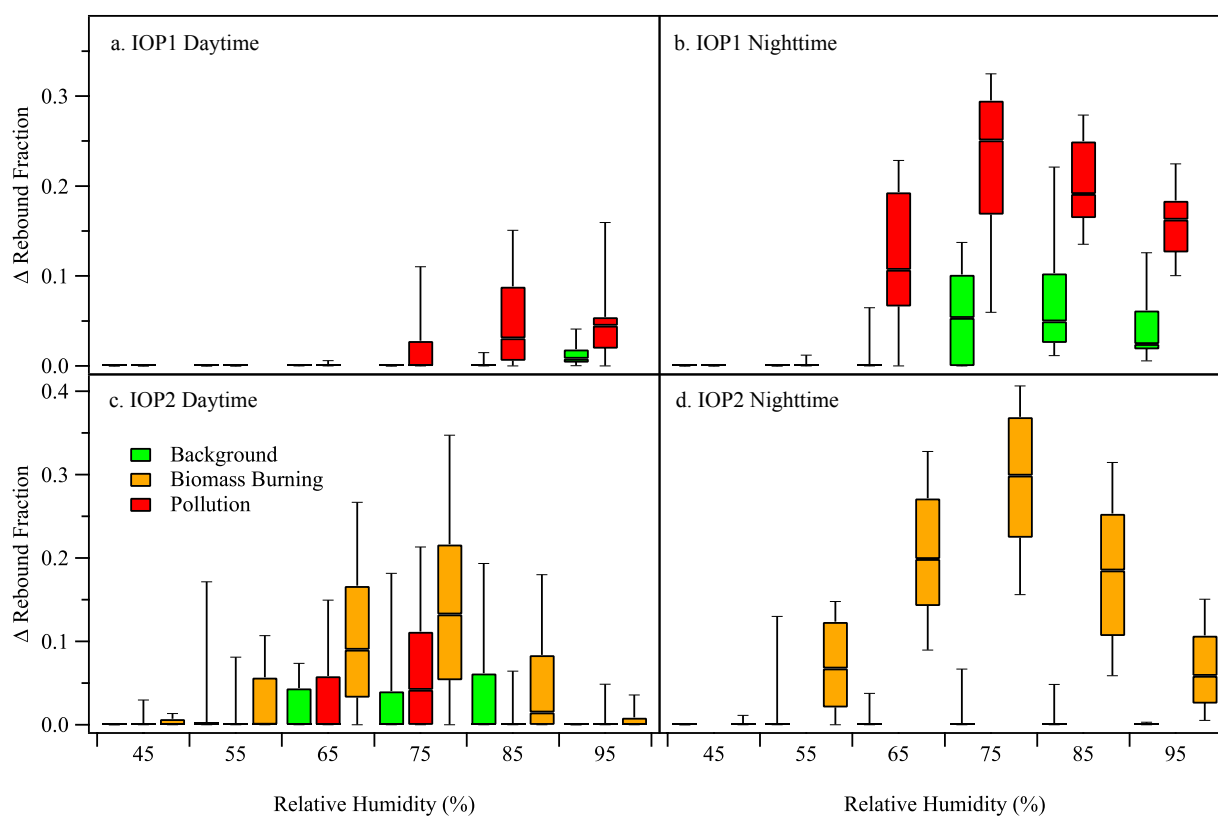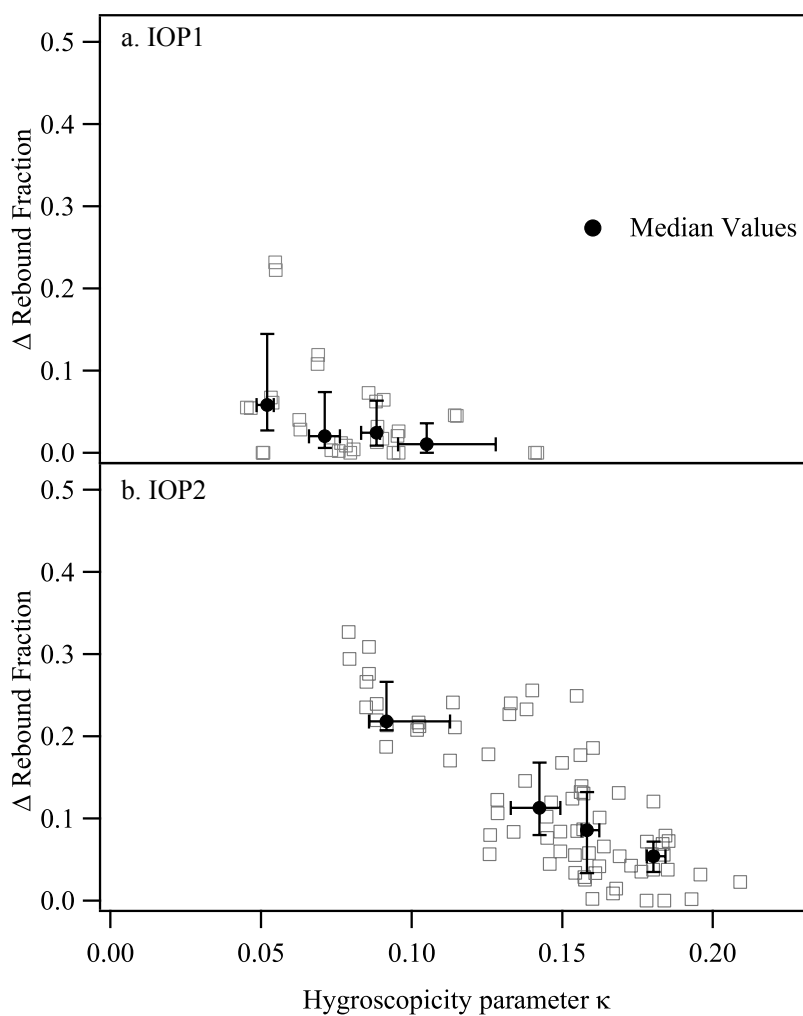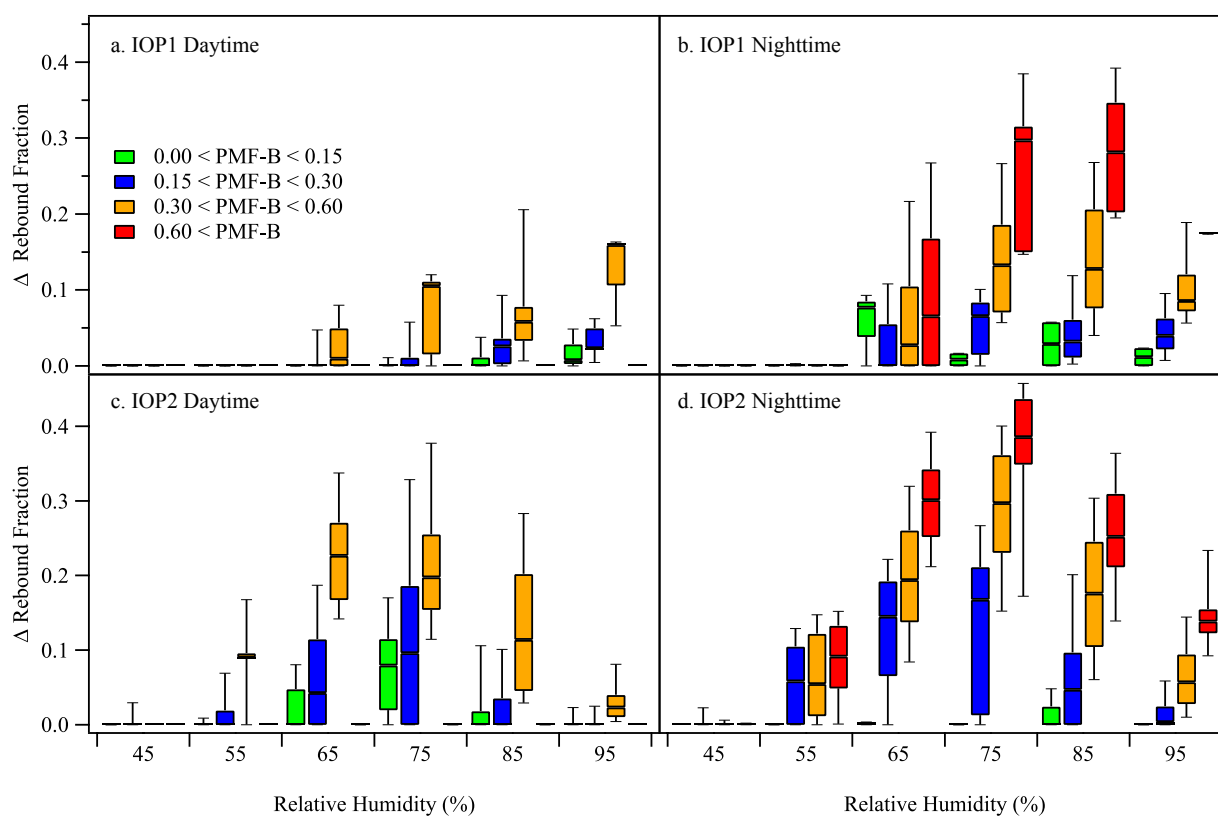Atmospheric
Chemistry
and Physics
Discussions

Figure 5

Atmospheric
Chemistry
and Physics
Discussions
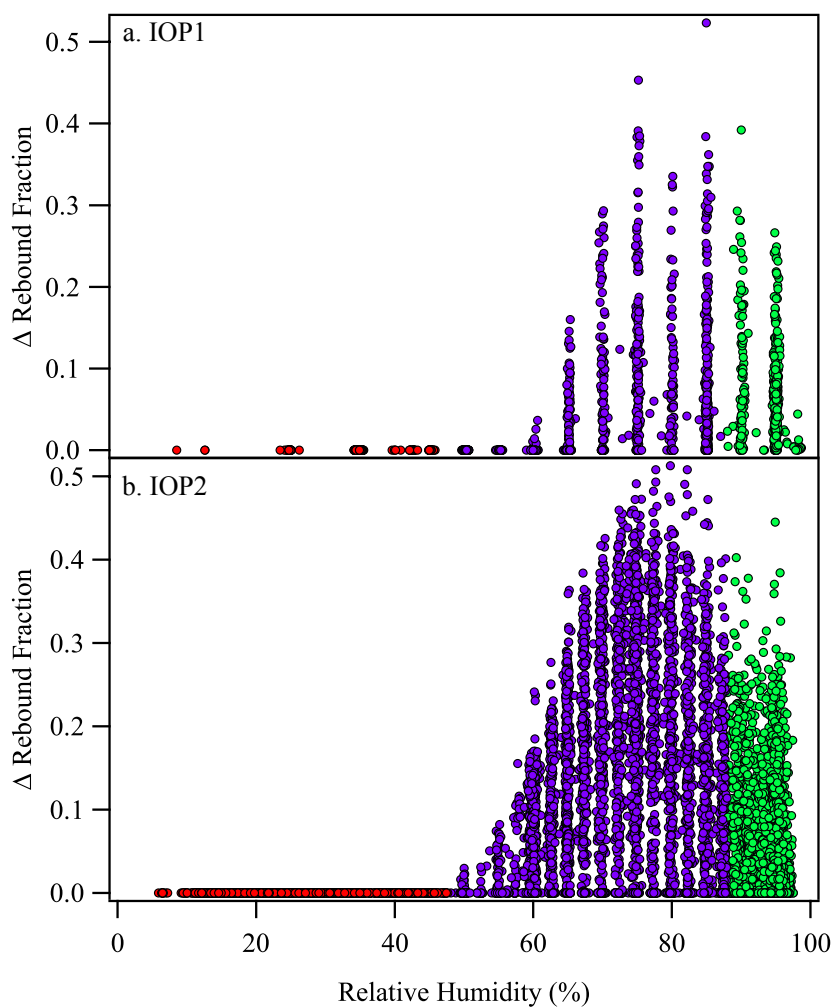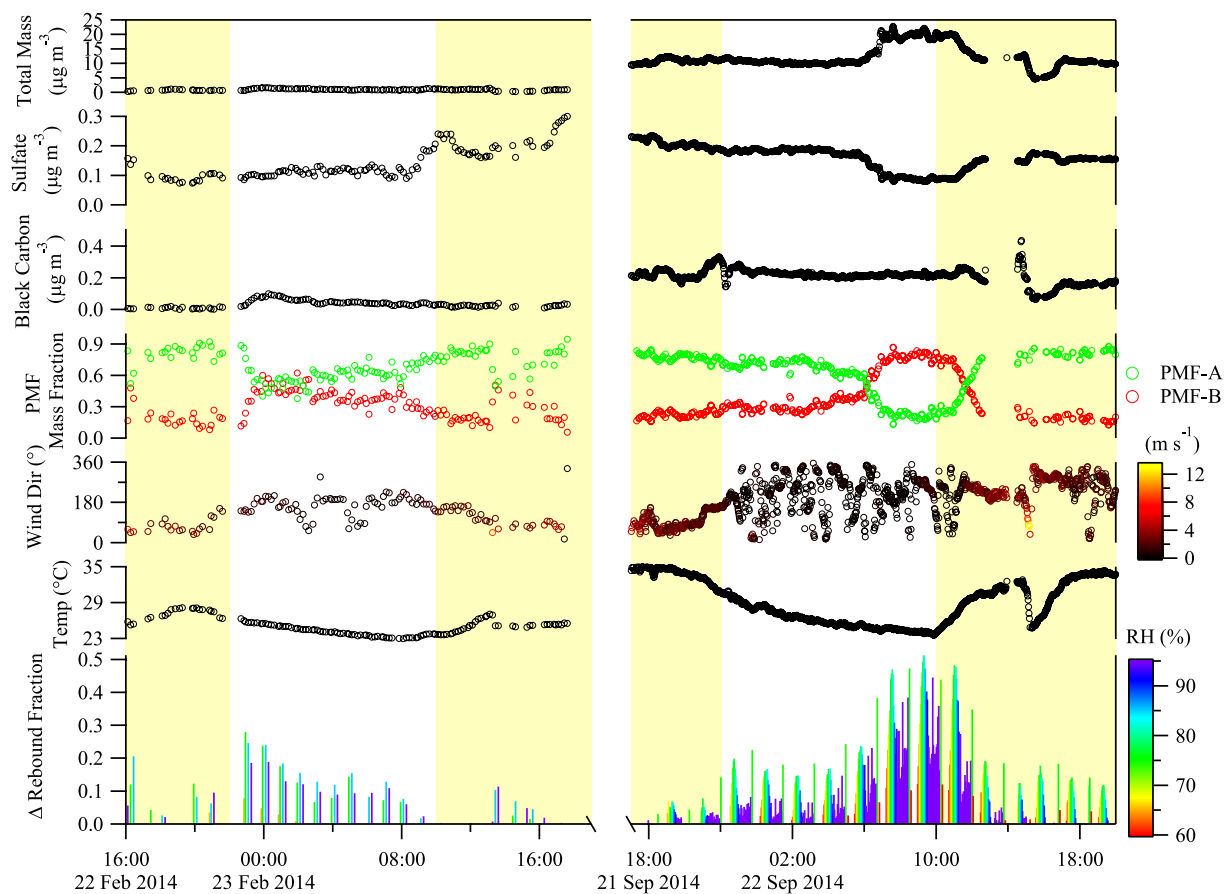
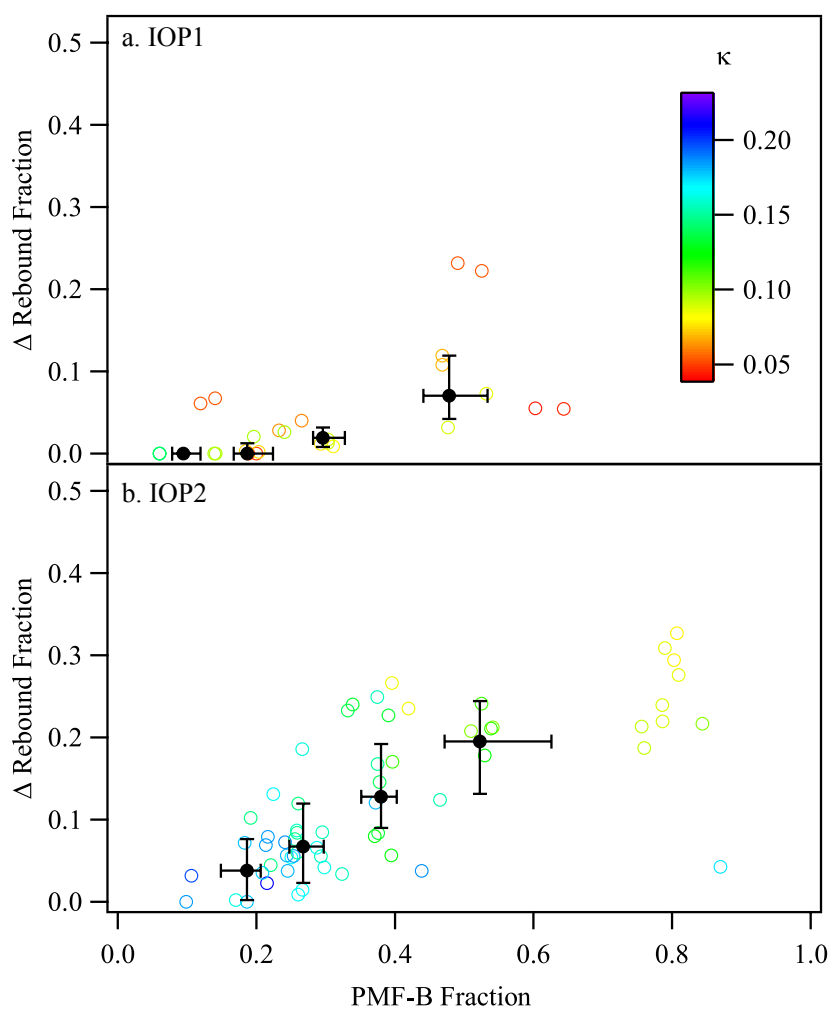Figure 6

Figure 7

Figure 8

Atmospheric
Chemistry
and Physics
Discussions

Open Access

Figure 9

Figure 10

Figure 11